

This is a repository copy of *RingSim—An agent-based approach for modeling mesoscopic magnetic nanowire networks*.

White Rose Research Online URL for this paper:

<https://eprints.whiterose.ac.uk/226667/>

Version: Published Version

---

**Article:**

Vidamour, Ian T., Venkat, Guru, Swindells, Charles et al. (9 more authors) (2025) *RingSim—An agent-based approach for modeling mesoscopic magnetic nanowire networks*. *Journal of Applied Physics*. 133901. ISSN 1089-7550

<https://doi.org/10.1063/5.0251692>

---

**Reuse**

This article is distributed under the terms of the Creative Commons Attribution (CC BY) licence. This licence allows you to distribute, remix, tweak, and build upon the work, even commercially, as long as you credit the authors for the original work. More information and the full terms of the licence here:

<https://creativecommons.org/licenses/>











**Takedown**

If you consider content in White Rose Research Online to be in breach of UK law, please notify us by emailing [eprints@whiterose.ac.uk](mailto:eprints@whiterose.ac.uk) including the URL of the record and the reason for the withdrawal request.



RESEARCH ARTICLE | APRIL 01 2025

## RingSim—An agent-based approach for modeling mesoscopic magnetic nanowire networks

Ian T. Vidamour ; Guru Venkat ; Charles Swindells ; David Griffin ; Paul W. Fry; Richard M. Rowan-Robinson ; Alexander Welbourne ; Francesco Maccherozzi ; Samjeet S. Dhesi ; Susan Stepney ; Dan A. Allwood; Thomas J. Hayward 



*J. Appl. Phys.* 137, 133901 (2025)

<https://doi.org/10.1063/5.0251692>



### Articles You May Be Interested In

A perspective on physical reservoir computing with nanomagnetic devices

*Appl. Phys. Lett.* (January 2023)

Voltage-controlled superparamagnetic ensembles for low-power reservoir computing

*Appl. Phys. Lett.* (May 2021)

Geometry of behavioral spaces: A computational approach to analysis and understanding of agent based models and agent behaviors

*Chaos* (November 2016)



Journal of Applied Physics

## Special Topics Open for Submissions

[Learn More](#)













# RingSim—An agent-based approach for modeling mesoscopic magnetic nanowire networks

Cite as: J. Appl. Phys. **137**, 133901 (2025); doi: [10.1063/5.0251692](https://doi.org/10.1063/5.0251692)

Submitted: 4 December 2024 · Accepted: 12 March 2025 ·

Published Online: 1 April 2025



Ian T. Vidamour,<sup>1,2,a)</sup>  Guru Venkat,<sup>1</sup>  Charles Swindells,<sup>1</sup>  David Griffin,<sup>3</sup>  Paul W. Fry,<sup>4</sup>  
Richard M. Rowan-Robinson,<sup>1</sup>  Alexander Welbourne,<sup>1</sup>  Francesco Maccherozzi,<sup>5</sup>  Sarnjeet S. Dhesi,<sup>5</sup>   
Susan Stepney,<sup>3</sup>  Dan A. Allwood,<sup>1</sup> and Thomas J. Hayward<sup>1</sup> 

## AFFILIATIONS

<sup>1</sup>School of Chemical, Materials, and Biological Engineering, University of Sheffield, Sheffield, United Kingdom

<sup>2</sup>School of Computer Science, University of Sheffield, Sheffield, United Kingdom

<sup>3</sup>Department of Computer Science, University of York, York, United Kingdom

<sup>4</sup>Centre for Nanoscience and Technology, University of Sheffield, Sheffield, United Kingdom

<sup>5</sup>Diamond Light Source Ltd., Science and Technology Facilities Council UK, Didcot, Oxfordshire, United Kingdom

<sup>a)</sup>Author to whom correspondence should be addressed: [i.vidamour@sheffield.ac.uk](mailto:i.vidamour@sheffield.ac.uk)

## ABSTRACT

We describe “RingSim,” a phenomenological agent-based model that allows numerical simulation of magnetic nanowire networks with areas of hundreds of micrometers squared for durations of hundreds of seconds, a practical impossibility for general-purpose micromagnetic simulation tools. In RingSim, domain walls (DWs) are instanced as mobile agents, which respond to external magnetic fields, and their stochastic interactions with pinning sites and other DWs are described via simple phenomenological rules. We first present a detailed description of the model and its algorithmic implementation for simulating the behaviors of arrays of interconnected ring-shaped nanowires, which have previously been proposed as hardware platforms for unconventional computing applications. The model is then validated against a series of experimental measurements of an array’s static and dynamic responses to rotating magnetic fields. The robust agreement between the modeled and experimental data demonstrates that agent-based modeling is a powerful tool for exploring mesoscale magnetic devices, enabling time scales and device sizes that are inaccessible to more conventional magnetic simulation techniques.

© 2025 Author(s). All article content, except where otherwise noted, is licensed under a Creative Commons Attribution (CC BY) license (<https://creativecommons.org/licenses/by/4.0/>). <https://doi.org/10.1063/5.0251692>

## I. INTRODUCTION

The creation of models of system behavior is critical to the development of emerging technologies since they allow for rapid evaluation of device designs without the need for manufacturing samples or performing experimental measurements. For devices based around magnetic materials, the processes that underpin the device’s response to external inputs often have simple analytical models. For example, devices, such as spin-torque nano-oscillators,<sup>1,2</sup> domain wall (DW) oscillators,<sup>3,4</sup> and super-paramagnetic ensembles<sup>5</sup> have one-dimensional numerical descriptions that allow the state of the magnetic substrate to be approximated to predict device performance quickly with low computation cost.

For devices that are not characterized well by simple analytical models, or when more detail of the underlying magnetic state of the

system is required, the typical approach is to use general-purpose micromagnetic simulation packages, such as MuMax3<sup>6</sup> or OOMMF.<sup>7</sup> These platforms approximate the spin structure of the magnetic materials into cells on the order of a few nanometers in size and model the evolution of spins via the Landau–Lifschitz–Gilbert equation.<sup>8,9</sup> While these simulation packages provide a high level of detail on the magnetic response of a device, they are associated with a high computational overhead. For example, in simulations of a skyrmion confined in a nanodisk of 80 nm diameter, 1 nm thickness, using a mesh size of 1 nm<sup>3</sup>, simulating 50 ms of dynamic response takes on the order of 40 min,<sup>10</sup> a simulation duration 48 000 times longer than the physical processes being simulated, despite the vast acceleration of these simulations possible with modern hardware.<sup>11</sup>

While magnetic systems with fast dynamics, such as spin-torque nano-oscillators, require simulations at the nanosecond/

14 May 2025 09:28:52



microsecond timescale, other systems with dynamics governed by thermal processes, such as the nanowire network presented here, may respond on much slower timescales and, hence, need orders of magnitude longer simulation durations. When coupled with the relatively larger size of these systems, micromagnetic simulation approaches become practically impossible. Despite these challenges, the huge design space of networks of interacting magnetic elements, such as artificial spin-ice systems<sup>12</sup> or arrays of interconnected magnetic nanorings,<sup>13</sup> makes exploration via simulations very attractive for prototyping new computational platforms. These systems also exhibit emergent behaviors, where interactions between elements in the system lead to global behaviors that cannot be described by the action of individual elements alone. While these complex dynamics provide technical difficulty for simulation, they can be exploited for neuromorphic computing purposes.<sup>14–21</sup> Therefore, it is clear that alternative approaches for modeling such systems must be taken.

Agent-based models provide a potential solution to these problems. These models describe the evolution of complex, multi-element systems in terms of the interactions between individual agents, as well as external environmental parameters.<sup>22</sup> The agents are often instantiated into the model with distributed parameters and commonly exhibit stochastic behaviors. Interactions between agents are programmed phenomenologically, with the outcomes of interactions determined by a set of predefined rules that aim to encapsulate the behaviors of the system being simulated. These types of models are especially harmonious with systems that exhibit emergent behaviors and have been used extensively in modeling complex dynamic systems, such as flocking birds<sup>23</sup> or even structures within the brain.<sup>24,25</sup>

In this paper, we introduce an agent-based model, RingSim, which allows rapid simulation of networks of thousands of interconnected magnetic nanorings over timescales on the order of seconds. The model simulates the stochastic pinning, depinning, and propagation of DWs at local pinning sites that occur at the junctions between rings in the arrays. DWs are instantiated as agents that interact with these pinning sites, as well as other DWs and externally applied magnetic fields. We fit model parameters describing ring junction properties and DW–DW interactions and show how the model produces excellence with experimental data. Not only is the model capable of capturing the system's global response to external inputs both statically and dynamically, but also provides information on the microstate of each ring, visually showing similar local agglomeration of domains and relative populations of individual ring states as observed experimentally.

## II. MAGNETIC NANORING ARRAY DYNAMICS

RingSim describes the emergent response of interconnected magnetic nanoring arrays [Fig. 1(a)], experimentally detailed in previous works.<sup>13,19,20</sup> Conceptually, the response of the system to rotating magnetic fields can be described via the transitions between a metastable domain configuration for each of the rings, mediated by stochastic pinning events. Figure 1(b) shows the three basic ring configurations: a “vortex” state containing a single domain and no DWs an “onion” state containing two equally sized domains and a pair of DWs at opposite ends of the ring, and a “three-quarter” state, featuring two differently sized domains, with

DWs situated at angles of 90° from one another. The interconnected nature of the ring arrays leads to local domain wall pinning sites at the junctions between neighboring rings. The change in geometry presented by the junction creates an energy barrier, similar to an “anti-notch,”<sup>26,27</sup> which tends to locally pin itinerant domain walls. When driven with sufficiently high amplitude rotating fields, the domain walls are able to overcome this energy barrier and coherently propagate with the rotating field, shown in Fig. 1(c1). Under smaller driving fields, domain walls can become locally pinned at these junctions, with a finite probability of depinning via thermal activation. These stochastic processes can lead to the domain walls within a single ring propagating differently depending upon the outcomes of pinning events. This in turn may then lead to domain wall collision and subsequent annihilation, changing the ring state from an onion/three-quarter state to a vortex state, shown in Fig. 1(c2).

Domain walls may also be reintroduced into the system when propagating domain walls lead to magnetic reversal across a junction. To avoid causing magnetic frustration when the magnetization of a junction is reversed, a pair of domain walls are nucleated in the ring adjacent to the propagating domain wall, shown in Fig. 1(c3). Between these mechanisms for domain wall annihilation and renucleation, a dynamic equilibrium is created between the rate of domain wall loss and gain, depending upon the relative probabilities of domain wall pinning/depinning for a given applied field.

At very low or very high applied fields, the pinning/propagation events are effectively deterministic, leading to few collisions, and hence, the array exists as mainly onion states with a few three-quarter states. For intermediate applied fields, the stochastic movement of domain walls leaves the array in a mixture of states from all three configurations depending upon the relative rates of collision and renucleation.

## III. MODELING STOCHASTIC PINNING EVENTS

The array behavior can be approximated via simulation of a domain state of each ring, determined by the outcomes of the pinning events. To achieve this, we use empirically verified relationships to calculate expected probabilities of domain walls in the system propagating beyond pinning sites. In magnetic materials, thermal energy introduces stochastic domain wall motion via the random fluctuation of individual magnetic moments, which assist reversal processes. This results in a finite expected timescale for a reversal event to occur, depending upon the size of the associated energy barrier and the temperature of the system. Empirically, the Arrhenius–Néel relationship calculates the characteristic timescale of reversal via Eq. (1),<sup>28</sup>

$$\tau_r = \tau_0 e^{\frac{\Delta E}{k_B T}}, \quad (1)$$

where  $\tau_r$  represents the expected reversal timescale,  $\tau_0$  the reciprocal of attempt frequency  $f_0$  associated with the material (here,  $f_0 \approx 1$  GHz for  $\text{Ni}_{80}\text{Fe}_{20}$ <sup>29</sup>),  $\Delta E$  the magnitude of the effective energy barrier,  $k_B$  the Boltzmann constant, and  $T$  the temperature of the system. This relationship has been experimentally verified for the reversal of single magnetic domains, with excellent agreement.<sup>30</sup>

As well as the temperature of the system, external magnetic fields also influence the outcome of pinning events by modulating



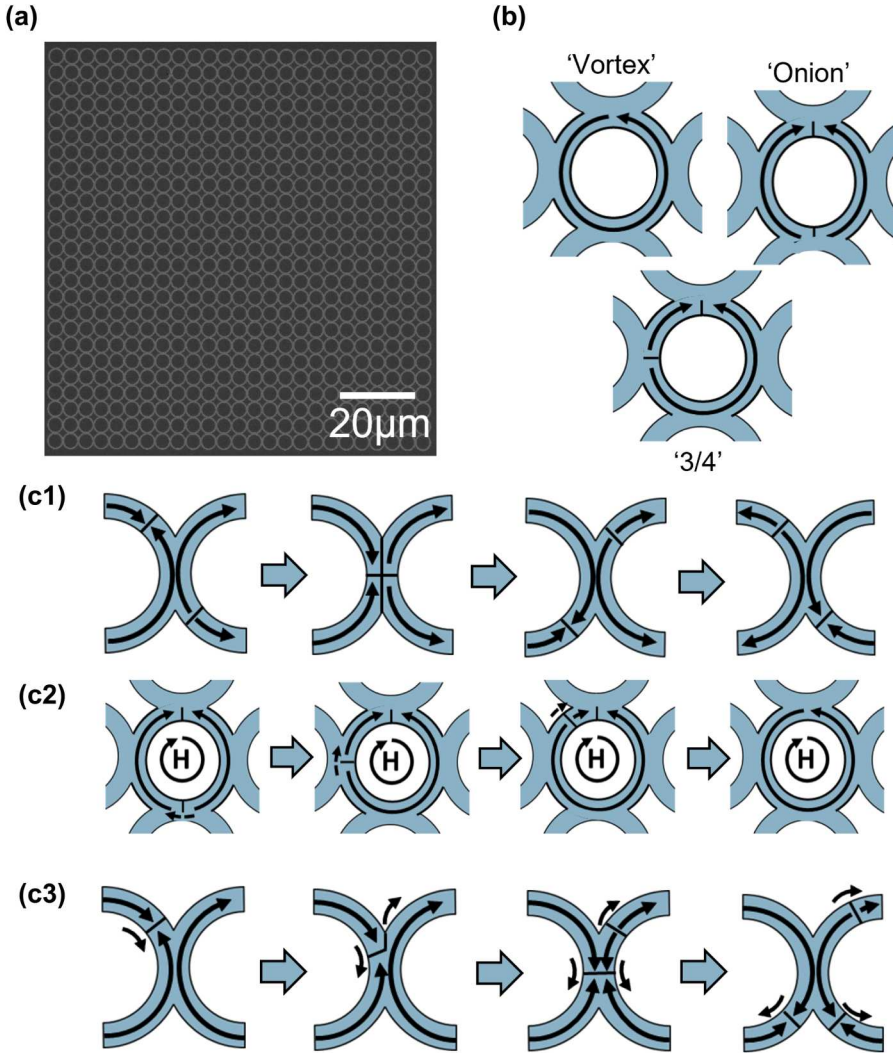


**FIG. 1.** (a) Scanning electron micrograph showing a  $25 \times 25$  magnetic nanoring array. (b) Schematic diagrams showing the three metastable domain states in an individual ring: Vortex configuration, onion configuration, and three-quarter configuration. Arrows show the direction of magnetization, and lines normal to the circumference of the rings reflect the position of domain walls. (c) Schematics showing the outcomes of different stochastic propagation events: (c1) Coherent propagation of DWs with sufficiently strong magnetic fields. (c2) Stochastic propagation of DWs within a ring, with the upper domain wall becoming locally pinned before being annihilated by the propagating lower domain wall. (c3) The renucleation process when an itinerant domain wall causes local magnetic reversal, injecting a pair of domain walls into an adjacent ring. Arrows show the magnetization direction, with lines reflecting domain walls. Dotted arrows included to show the propagation direction of domain walls, and large blue arrows represent the progression of time.

14 May 2025 09:28:52

the magnitude of the effective energy barrier. Previous work has shown that this modulation is dependent upon the component of an applied field acting tangentially to the ring at the position of the domain wall, with the domain walls having the lowest Zeeman energy when aligned with the field vector.<sup>31,32</sup> The rotating magnetic fields used to drive the ring arrays means that this transverse component,  $H_{\text{transverse}}$ , is dependent upon the magnitude of the applied field,  $H_{\text{applied}}$ , and the angle between the applied field and the domain wall,  $\theta_{\text{lag}}$ , shown schematically in Fig. 2(a) and described mathematically via

$$H_{\text{transverse}} = H_{\text{applied}} * \sin(\theta_{\text{lag}}). \quad (2)$$

The relationship between the transverse field, the magnitude of the modulated energy barrier,  $\Delta E$ , and the zero-field barrier,  $E_0$ , is given via the phenomenological Sharrock equation,<sup>33</sup>

$$\Delta E = E_0 \left( 1 - \frac{H_{\text{transverse}}}{H_{\text{sw}}^0} \right)^\alpha, \quad (3)$$

where  $H_{\text{sw}}^0$  represents the zero-Kelvin switching field of the magnetic element and  $\alpha$  is a geometrical constant (here taken to be  $3/2$ <sup>34</sup>).

It has been observed in previous works that the presence of either one or two domain walls across a junction leads to different domain wall structures,<sup>13</sup> each with different energetic properties, and, hence, different depinning behaviors. Here, we assume that  $E_0$  and  $H_{\text{sw}}^0$  for the single and double domain wall case are related as follows:

$$H_{2\text{DW}}^0 = k * H_{1\text{DW}}^0, \quad (4)$$

$$E_{2\text{DW}}^0 = k * E_{1\text{DW}}^0, \quad (5)$$



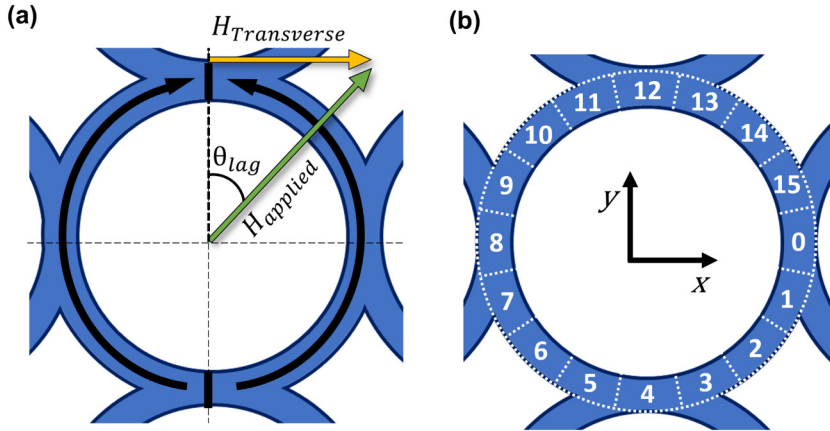


**FIG. 2.** (a) Schematic diagram showing the calculation of  $H_{\text{transverse}}$  from an applied field  $H_{\text{applied}}$  and the angular lag between the domain wall location and the direction of the applied field,  $\theta_{\text{lag}}$ . (b) Schematic diagram representing the cardinal X and Y axes directions, as well as the corresponding junction indices at each of the intersections between the rings for  $N_{\text{segment}} = 16$ .

where  $H_{1\text{DW}}^0$  and  $H_{2\text{DW}}^0$  represent the switching fields for one and two domain wall cases, respectively,  $E_{1\text{DW}}^0$  and  $E_{2\text{DW}}^0$  the equivalents for initial energy barriers, and  $k$  a fixed scaling parameter, the fitting of which is discussed in Sec. V.

There are two key assumptions made here for simplicity of the model: (a) that  $E_0$  and  $H_{\text{sw}}$  for the 1 and 2 DW cases vary similarly and (b) that these variations are linear. While these assumptions lead to models that can accurately reproduce experimental data for the system studied here (shown in Sec. VI), they are likely to not hold for systems where these parameters show distinct, complex variations. In these cases, further exploration into how both  $E_0$  and  $H_{\text{sw}}$  vary for the different DW configurations, for example, via micromagnetic simulations, can establish a more accurate description of these variations.

In order to approximate the varying  $H_{\text{transverse}}$  (and, consequently,  $E_0$ ) as the applied field rotates, the field is discretized into a series of angular steps, each held for a duration of  $t_{\text{step}} = \frac{N_{\text{steps}}}{2\pi f}$  s, where  $N_{\text{steps}}$  represents the number of discretization steps per rotation and  $f$  represents the rotational frequency of the applied field. This allows the approximated depinning probability for a domain wall in a given discretization step,  $P_{\text{depin}}$ , to be calculated from Eqs. (1)–(5) via Eq. (6),

$$P_{\text{depin}} = 1 - e^{-\frac{t_{\text{step}}}{\tau_r}}. \quad (6)$$

#### IV. PHENOMENOLOGICAL MODELING OF MAGNETIC NANORING ARRAYS

Phenomenological descriptions of domain walls and their interactions allow a simple method for programming experimentally observed propagation, annihilation, and nucleation behaviors. Parameters describing properties of rings, junctions, and numbers of elements have labels R, J, and N, respectively.

In the model presented here, domain walls are instanced as agents of a single class, representing a vortex domain wall structure (VDW) with associated field and energy parameters that govern their depinning behaviors. For the geometry studied here, VDWs represent the large majority of DWs observed in the system.<sup>13</sup>

However, for different geometries with a more diverse range of DW configurations, the DWs in the system should be modeled via further classes with distinct parameters to produce a more complete description of the diverse dynamical behaviors.

The rings within the model are represented by vectors of length  $N_{\text{segment}}$ , where each entry to the vector represents a ring segment of arc length  $2\pi/N_{\text{segment}}$  radians. The indices of this vector each represent a position within the ring, rotating clockwise from the positive x direction, shown in Fig. 2(b). Here, a value of 16 for  $N_{\text{segment}}$  was selected to provide a good trade-off between approximating a smooth rotation of field and matching the four-fold symmetry of the array, while keeping the number of simulation steps low.

The domain state of the nanoring array,  $R_{\text{DW}}$ , is expressed as a matrix of dimensions  $[N_{\text{segment}} \times (N_r)^2]$ , where  $N_r$  represents the number of rings in each row of the square array. Domain walls are instanced into the array by labeling an index in each ring vector with either a +1 or a -1, reflecting head-to-head and tail-to-tail domain walls, respectively. Since many of the key behaviors of the ring array are determined by the junctions between the rings in the array and the interactions that arise at them, three separate vectors of length  $2N_r(N_r - 1)$  are created, which record the properties of every junction in the network:  $J_{\text{DW}}$ , which tracks the number of domain walls occupying each junction;  $J_E$ , which reflects the magnitude of the energy barrier  $E_0$  presented by each junction; and  $J_H$ , which reflects the zero-kelvin switching field  $H_{\text{sw}}^0$  for each junction, as described in Sec. III.

The state of the simulated nanoring array is initialized by instancing a head-to-head domain wall in every ring in  $R_{\text{DW}}$  at index  $\frac{N_{\text{segment}}}{4}$ , and a tail-to-tail domain wall in every index  $\frac{3 \times N_{\text{segment}}}{4}$ , corresponding to the positive/negative y direction, respectively, and emulating the saturated state of all onion state rings aligned in the positive y direction. The magnetization state of the array is then generated from the position and variety of all domain walls in the system. First, an additional array,  $R_{\text{dir}}$ , of an identical shape to  $R_{\text{DW}}$  is generated. This array records whether the magnetization runs clockwise (+1) or anticlockwise (-1) over each segment and is marked zero in the locations of domain walls.

14 May 2025 09:28:52



From this direction array, the net magnetization of the array may be calculated in terms of components in the  $x$  and  $y$  axes ( $M_x$  and  $M_y$ , respectively) via

$$M_x = \sum_{i=1}^{N_r^2} \sum_{s=1}^{N_{\text{segment}}} \sin\left(\frac{2\pi s}{N_{\text{segment}}}\right) R_{\text{dir}}^{i,s} \quad (7)$$

$$M_y = \sum_{i=1}^{N_r^2} \sum_{s=1}^{N_{\text{segment}}} \cos\left(\frac{2\pi s}{N_{\text{segment}}}\right) R_{\text{dir}}^{i,s}. \quad (8)$$

This gives the magnetization of the array in arbitrary units, which is then normalized against the magnetization in the saturated state, determined as the value of  $M_y$  in the initialized array.

Figure 3(a) shows how the model evolves the magnetic state of the system: First, the external applied field is moved by a fixed angular step. The relative probabilities of all domain walls in the system depinning are then calculated via Eqs. (1)–(6) and compared with a random variable drawn from a uniform distribution between 0 and 1 to determine which domain walls are free to propagate. The domain walls then propagate toward their respective energy minima along the field vector, potentially interacting with other domain walls and junctions as they move.

Figure 3(b) shows a flow chart for the process of calculating depinning probabilities. In RingSim, two sources of domain wall pinning are considered: pinning due to edge roughness and pinning at junctions. The effects of edge roughness are included by imposing a threshold field, below which domain wall propagation does not occur.<sup>35</sup> This information is stored within a vector representing the edge roughness threshold field for each ring,  $R_{\text{ER}}$ , created by sampling from a normal distribution with a fixed mean and standard deviation to resemble the expected variance in properties via manufacturing imperfections in experimental samples. The exact mean and variance were determined via correlation with experimental data as discussed in Sec. V. This acts as a hard threshold by setting depinning probability to zero if  $H_{\text{transverse}}$  [via Eq. (2)] is below the value of  $R_{\text{ER}}^i$  for a given ring  $i$ .

Domain wall pinning at junctions is modeled as follows: Domain walls occupying the same junction are considered coupled in RingSim, with the calculation of reversal probabilities occurring only once with coupled outcomes for both domain walls. The number of domain walls at each junction is given by the entry in  $J_{\text{DW}}$  for a particular junction. Each junction has its own energy barrier and switching field, stored in the vectors  $J_E$  and  $J_H$ , which are scaled for domain wall–domain wall interactions via Eqs. (4) and (5) if two domain walls occupy the junction. The effects of the external field are accounted for by scaling the energy barrier via Eq. (3), giving the magnitude of the effective energy barrier  $\Delta E$ . As the depinning process is thermally activated, the expected transition time for reversal is determined via Eq. (1). The rotational frequency of the applied field is then used to give an expected probability of reversal for a given angular step, described via Eq. (6).

Figure 3(c) shows a flow chart for determining whether a domain wall depins during a given step of the model. A random number sampled from a uniform distribution between zero and one,  $x$ , is generated for each junction and is compared to  $P_{\text{depin}}$ . Domain walls occupy any junction where  $P_{\text{depin}} > x$  are deemed

free to propagate. The process for domain wall propagation is outlined in Fig. 3(d). Depinned domain walls propagate either clockwise or anticlockwise according to the shortest route to their respective energy minima. If the propagation of a domain wall would lead to magnetic frustration across a junction, then the nucleation process occurs. A pair of domain walls, one head-to-head and one tail-to-tail, are initialized at the junction in the adjacent ring. The domain wall closest to its respective energy minimum moves directly to this location. The other domain wall is then flagged for an additional depinning check at the junction where it was initialized. In the case where both minima are equidistant from the initialization junction, both domain walls propagate to their respective minima where they remain until the next field step.

In a given ring, domain walls propagate toward their energy minimum until one of the three conditions are met: (a) If they collide with another domain wall before reaching their respective minimum, the domain walls annihilate and leave the ring in a vortex state. (b) If the domain wall reaches another junction before its energy minimum, then the domain wall is flagged for an additional depinning check at that junction since it may become locally pinned again. (c) If the domain wall reaches its energy minimum, it remains there until the next field step.

After propagation has occurred, the junctions are then checked for the number of domain walls occupying them, and the  $J_{\text{DW}}$  vector is updated accordingly. The magnetization state of the array is then calculated from the final positions and returned in terms of normalized  $M_x$  and  $M_y$  components, and all state matrices are updated. The field then moves another angular increment, and the process starts over.

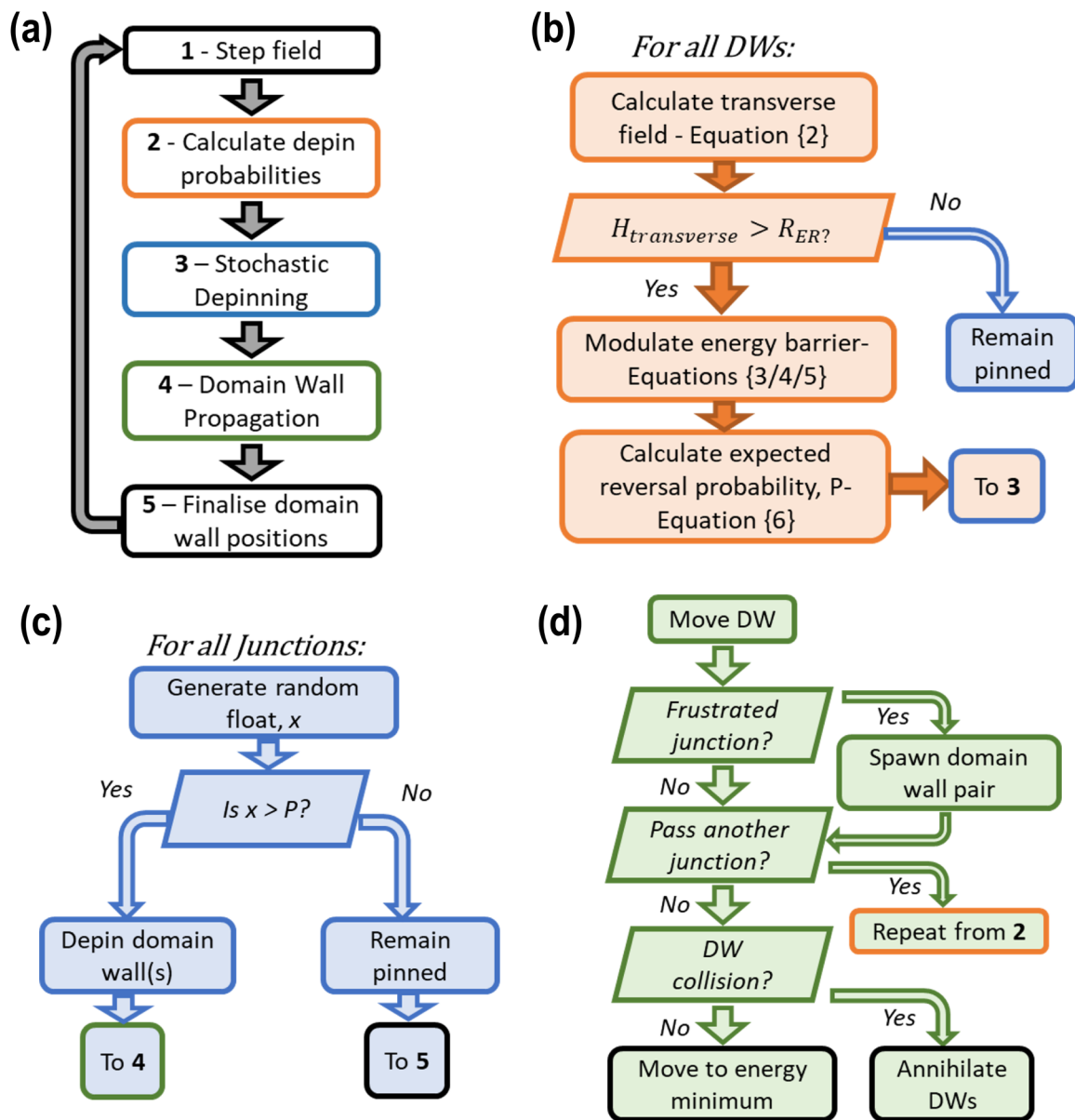
## V. FITTING MODEL PARAMETERS

RingSim has a number of free parameters that must be appropriately selected to recreate experimental behaviors. Here, data are gathered from (and the model fitted to reflect) manufactured devices with nominal diameters of 4  $\mu\text{m}$ , track widths of 400 nm, thicknesses of 10 nm, and with each ring overlapping 50% of its track width with its neighbor. Values of  $\tau_0$  and  $\alpha$  were taken from the literature, as an attempt frequency of 1 GHz for a Permalloy,<sup>29</sup> and an alpha value of 3/2.<sup>34</sup>

Fitting data, gathered both experimentally (steady-state response via AMR at various temperatures) and via micromagnetic simulations (1DW vs 2DW depinning field variation), were taken prior to the fitting of the model, with these results used to determine model parameters. Further data were gathered after calibrating model parameters (measurements of timescales of decaying response via AMR and X-PEEM data on microstate formation), which were and used to validate the fit established here with no further tuning of model parameters. This validation is shown in Sec. VI.

To establish the effects of domain wall–domain wall interactions on the switching field of the junction in the absence of thermal effects, micromagnetic simulations using the MuMax3<sup>6</sup> software package were performed on a pair of overlapping half-rings, representing a single junction, but extending to ring properties via symmetry. Material parameters of the system were set to reflect  $\text{Ni}_{80}\text{Fe}_{20}$  in line with the manufactured devices





14 May 2025 09:28:52

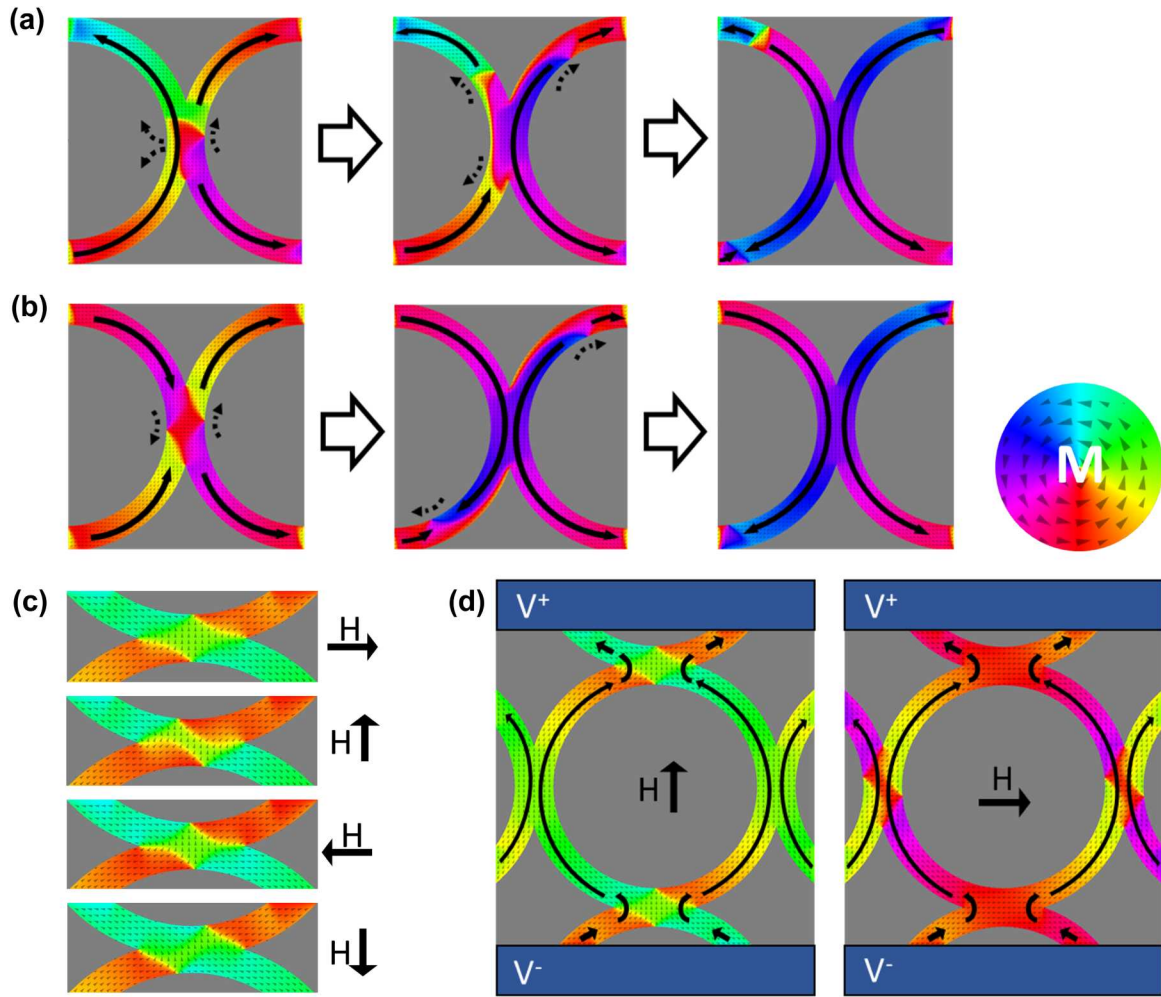
**FIG. 3.** (a) Overview of the key steps taken in the modeling procedure. (b) Process for determining the probabilities  $P$  for each of the domain walls to propagate within the model. (c) Process for deciding the stochastic outcomes of pinning events based on previously calculated probability  $P$ . (d) Process for determining the next state of the array from the outcome of depinning events and any collisions or additional junctions that may be passed on the domain wall's path to the energy minimum.

( $M_s = 860$  kA/m,  $A_{ex} = 13$  pJ/m), with an artificially large damping parameter,  $\alpha_G = 1$ , to speed up simulation convergence. The simulations, shown in Figs. 4(a) and 4(b), were initialized with a single domain wall and two domain walls occupying the junction, respectively, and field tangential to the junction was ramped in 1 Oe increments every 8 ns. The domain walls were deemed to depin at the field when they became fully delocalized from the junction, and the strength of the applied field recorded, with

depinning fields of 79 and 64 Oe observed for the one and two domain wall cases, respectively.

While these results reflect the zero-kelvin switching field for an idealized material, imperfections from the manufacturing process (lower true saturation magnetization, imperfect geometry, presence of grains, etc.) mean that these values will not be numerically identical to those of a manufactured device. However, these values were used to be indicative of the ratio





14 May 2025 09:28:52

**FIG. 4.** (a) and (b) Domain wall reversal processes for one and two domain wall cases, respectively, produced using MuMax3. Black arrows show the direction of domains, and white arrows reflect increasing of the applied field. (c) MuMax simulations of a domain wall structure across a junction during applications of a 20 Oe rotating field in  $\pi/2$  radian steps, showing the expansion and contraction of the domain wall via magnetic susceptibility. (d) MuMax simulations of a domain state with domains pinned in orientations parallel to the current density (left) and orthogonal to the current density (right). Black arrows reflect the flow of the current density. Color wheel reflects the direction of magnetization in all plots, with the local direction shown by gray triangles on the color wheel.

between the two processes and, hence, used to determine the value of  $k$  in Eq. (4). As highlighted in Sec. III, the scaling of the energy barriers was assumed to be equivalent, giving a  $k$  value of 0.81 for Eqs. (4) and (5).

The remaining free parameters of  $R_{ER}$ ,  $E_0$ , and  $H_{sw}^0$  were fit to magnetoresistance (AMR) measurements of the nanorings. As described in previous works,<sup>20</sup> the AMR response of the nanoring array has two distinct responses to rotating fields: one at the frequency of the rotating field (1f response) and another at twice the field frequency (2f response). The 1f response occurs due to susceptibility effects, with elastic stretching and contraction of the domain walls in the system in response to the rotating field [Figure (c)]. The 2f signal depends upon the propagation of domain walls as they move between junction sites where pinned

domain walls sit either orthogonal or parallel to the current density [Fig. 4(d)].

Figure 5(a) shows the relative magnitudes of the Fourier components of the AMR response of the 1f and 2f frequency components across a range of applied fields over 30 rotations. Two key features of this response were used to fit model parameters: First, the end of the linear regime of the 1f response reflected the onset of domain wall motion, as the change from a linear increase is due to the addition of incomplete propagation of domain walls around the rings. This allows determination of the mean value of  $R_{ER}$  as 20.5 Oe. Second, the magnitude of the 2f signal reflects the number of domain walls propagating in the system. This is proportional to the amplitude of the net magnetization oscillations of the array for a given rotation, which was given by  $M_x$  and  $M_y$  in RingSim. This



equivalence allowed tuning of the remaining free parameters of  $E_0$  and  $H_0$  by comparing the amplitude of the magnetization output in RingSim to the experimental 2f data for the same applied fields and selecting  $E_0$  and  $H_0$  values, which provide the same response. The experimental procedure used to generate the 2f data in the experiment (30 rotations of applied fields between 25 and 30 Oe) was simulated in RingSim for a series of initializations spanning a range of  $E_0$  and  $H_0$  values.

Figures 5(b) and 5(c) show the magnitude of the oscillating  $M_y$  signal from RingSim over a few example  $E_0$  and  $H_0$  pairs with

respect to the applied field compared with the device's 2f response and the mean-squared error between the simulated magnetization and the experimental response across all  $E_0$  and  $H_0$  pairs, respectively. It can be observed that a band of  $E_0$  and  $H_0$  pairs are able to fit the experimental data well, reflected by the region of a low mean-squared error in Fig. 5(c).

Since the temperature also modulates the relative depinning probabilities, which determine the number of propagating domain walls, the AMR response of the experimental system over a range of applied temperatures must also be determined to find the

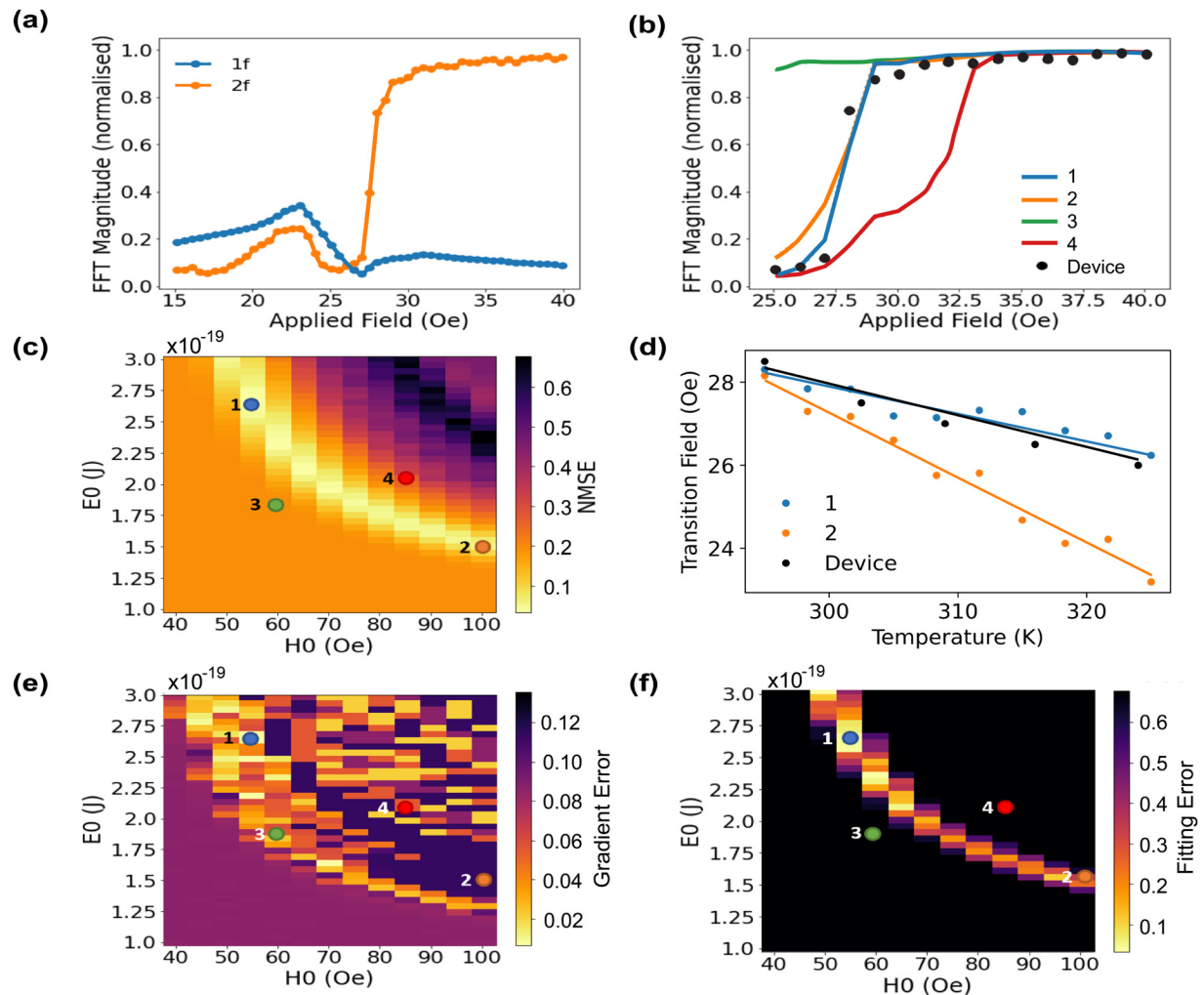


**FIG. 5.** (a) Normalized magnitudes of Fourier components corresponding to the clock frequency (1f) and twice the clock frequency (2f) over 30 rotations of varying magnetic fields. (b) Example fits of the RingSim magnetization output to the 2f transition in an experimental device. The four colored lines reflect different  $E_0/H_0$  pairs, shown in the map in (c). (c) Colormap of a mean-squared error between model's reproduction of magnetization and an experimentally gathered response via AMR for all explored  $E_0/H_0$  values. (d) Plot of extracted transition fields by varying the temperatures of the magnetic ring array for the experimental device (black) and promising initial fits 1 (blue) and 2 (orange). The transition field determined from the point of maximum gradient in the 2f response, with a linear fit used to extract the change in the transition field with the temperature shown. (e) Colormap showing gradient of the transition field with respect to the temperature, shown for all  $E_0/H_0$  pairs. (f) Combined fitting metric made by combining the difference in the gradient of the transition field between the simulated system and the experimental system and the mean-squared error between the simulated 2f transition and experimental data.



specific  $E_0$  and  $H_0$  pair that describes the system best. The temperature of the system was controlled by mounting the device on a Peltier cell, with the temperature measured via a pyrometer positioned above the device. From these measurements, a linear shift in the point of the maximum gradient of the  $2f$  response, hereon termed the “transition field,” was observed and shown in Fig. 5(d). Similarly to the previous fitting process, these experiments were repeated within RingSim, and the gradient of this linear shift calculated across a range of  $E_0$  and  $H_0$  pairs and compared to the experimentally gathered data. To determine the magnitude of the shift of characteristic transition points with respect to the temperature, the point of the maximum gradient in the  $2f$  transition in experiments (or the  $M_y$  amplitude in RingSim) was chosen. Crucially, the error between simulated and experimentally measured gradients of the shift in the transition field with increasing temperature shown in Figs. 5(d) and 5(e) is different when compared to the  $2f$  fit shown in Fig. 5(c). This highlights that while fit (2) produces an accurate representation at 298 K, the variation in response due to increasing temperature is incorrect with this fit. This additional constraint enabled selection of a single  $E_0$  and  $H_0$  pair from the range of

viable solutions in Fig. 5(c). An optimal  $E_0$  and  $H_0$  pair was chosen, which reconciles both experiments, here determined to be  $H_0 = 55$  Oe and  $E_0 = 2.625 \times 10^{-19}$  J (point “1” in Fig. 5).

## VI. VALIDATING THE MODEL

Section V outlined a procedure for fitting model parameters to the AMR response of the rings following 30 rotations of the applied field, where the DW population was expected to have reached an equilibrium. However, the ring arrays are known to exhibit complex transient dynamics over several rotations of the applied field, as well as different microstate populations of the three ring domain states [Fig. 1(b)] with respect to the driving field.<sup>13</sup> Thus, to confirm that the model also captures these behaviors, the model’s predictions were validated against additional experimental data taken after fitting the model that measures the dynamic timescales of the system’s response, as well as the populations of domain states observed experimentally. These results show that the model fitted on preliminary data extends to further behaviors of the physical system.

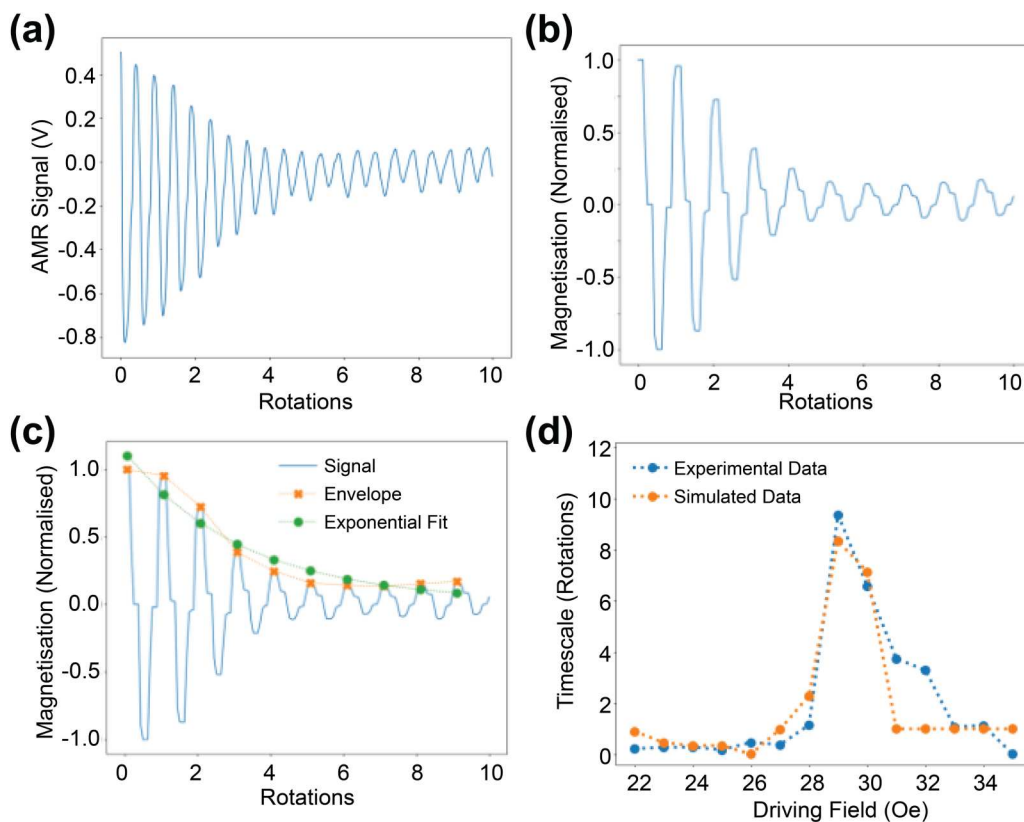


**FIG. 6.** (a) Measured voltage signal from the experimental measurement of the ring devices under 10 rotations of the 29 Oe applied field. (b) Simulated magnetization response via RingSim for 10 rotations of the 28 Oe applied field. (c) Outline of the procedure for measuring dynamic timescales. First, the envelope of the underlying signal is generated by marking the maximum magnetization over a rotation of the applied field, shown by the orange markers. Then, an exponential fit is generated to replicate the envelope of the magnetization/AMR signal, shown in green. (d) Comparison of the resulting decay timescales for experimentally gathered data (blue) and the simulated magnetization output (orange). The timescale is presented with respect to the number of rotations rather than in time.

14 May 2025 09:28:52



To establish the dynamic behaviors of the physical system, further AMR measurements were performed to determine the rate at which the ring array reaches a dynamic equilibrium in its AMR response from a saturated state over a range of applied fields. Figures 6(a) and 6(b) show the AMR response of the physical device at 29 Oe and the equivalent magnetization response generated by RingSim, respectively. Although the RingSim magnetization response occurs at half the frequency of the AMR response, the signals are very similar in terms of decay time and the magnitude of oscillations at equilibrium. In order to evaluate these dynamic timescales  $\tau_d$ , the envelope of the AMR was calculated over successive rotations, and an exponential function of the form  $X(t) = X_0 - ae^{-\frac{t}{\tau_d}} + c$  was fitted to the resulting decay curve. This was compared to a similar exponential fit to the envelope of the magnetization signal generated by RingSim, shown in Fig. 6(c).

Figure 6(d) shows the comparison between the fitted  $\tau_d$  parameters across these fields for both simulated and experimental data. There is excellent agreement between the simulation and experiments, showing that RingSim effectively simulates the regions of highly stochastic propagation well, and corroborating the presence of the longest timescale at  $H = 29$  Oe. However, there are longer timescales observed  $H = 30$ – $32$  Oe in experiments than in simulation, with the simulation predicting the equilibrium amplitude reaching instantaneously. This suggests that RingSim underestimates the field at which domain walls deterministically overcome pinning and magnetization oscillates at a maximum amplitude. Further evidence of this can also be observed in Fig. 5(b) where the best-fit data from RingSim saturated more quickly than the experimental FFT magnitude.

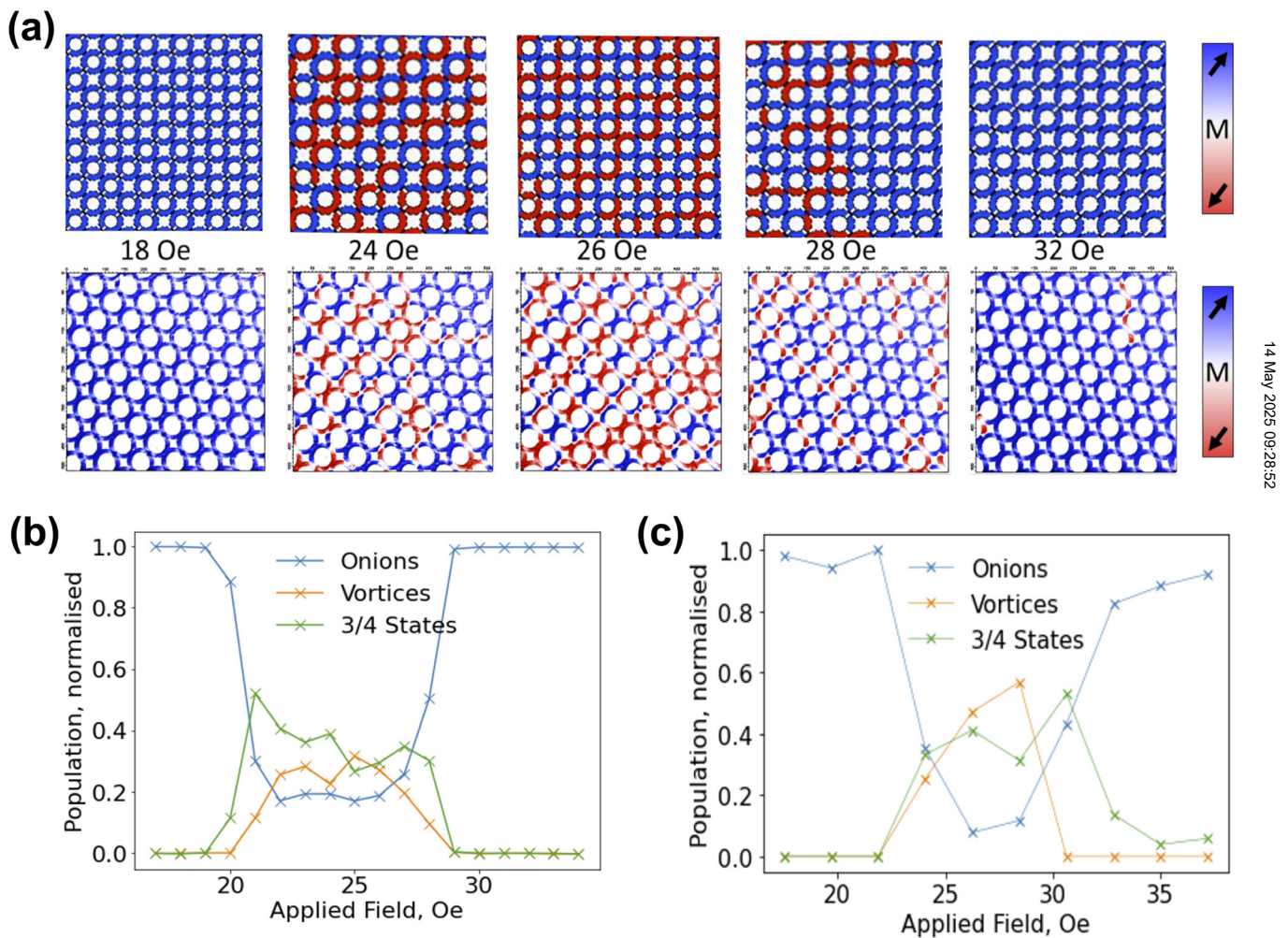


**FIG. 7.** (a) Comparison of the magnetization state between ring structures generated via RingSim (upper) and experimentally gathered data via X-PEEM imaging (lower) for applied fields between 18 and 32 Oe. In both cases, color reflects the magnetization direction along the vertical axis, reflected in the color bar on the right. (b) State count of the three different ring domain configurations (onion, vortex, and three-quarter) with respect to the magnitude of the simulated rotating field. Generated over a  $25 \times 25$  array, normalized against the ring number. (c) State count of ring domain configurations with respect to the magnitude of current provided to driving the electro-magnet.<sup>37</sup> Generated over subsection of the  $25 \times 25$  ring array containing 40–50 nanorings, normalized against the ring number for a given image.



To explore the microstates formed by the ring array, X-ray photo-emission electron microscopy (X-PEEM) was performed on subsections of the nanoring array at Beamline I06 at Diamond Light Source, UK. These measurements were performed by initializing the array to “onion” state rings with a strong pulse of the magnetic field, before driving with 30 rotations of applied fields at varying strengths. Images of the resulting domain state were generated by averaging a series of X-ray absorption (XAS) images on and off the Fe-L<sub>3</sub> resonance with clockwise and anti-clockwise polarized x rays, generating contrast according to the magnetization direction via X-ray magnetic circular dichroism (XMCD). Figure 7(a) (upper) shows example X-PEEM micrographs of the arrays at various applied fields.

To validate these behaviors in RingSim, a visualization tool was developed, which emulates the magnetic contrast observed in X-PEEM according to the values of  $M_z$  in each segment of all of the rings in the simulated system. The experimental procedure outlined for X-PEEM (saturation, 30 rotations of the applied field) was repeated within RingSim and compared with images generated via the visualization tool. Figure 7(a) compares images measured by XPEEM with those generated by RingSim at five different applied fields. RingSim shows similar grouping of larger domains locally, reflecting a similar tendency for the domain wall–domain wall interactions in both the physical device and within RingSim to lead to local regions of magnetic order, suggesting that RingSim is able to encapsulate the emergent behaviors observed in experiments.

To quantify the relative proportions of vortex, onion, and three-quarter state rings from the previous images, a custom image processing library within Python<sup>36</sup> was used to identify each of the ring states and count their populations. In RingSim, populations were determined from the number and locations of domain walls within the model. Figures 7(b) and 7(c) show the variation of these populations for simulated  $25 \times 25$  ring arrays and experimentally gathered data on a sub-sample of the  $25 \times 25$  array, respectively. RingSim captures the general population trends for the ring states with respect to the applied field well. However, there is some variance between the relative populations observed in experiments and simulated by RingSim.

One possible source of the differences between the X-PEEM measurements and the RingSim model is that the sample used for X-PEEM is different from the sample used for fitting the model. Although the nominal dimensions of the arrays’ designs were the same, they were manufactured in different lithography and deposition runs from the electrically contacted arrays, which could lead to some slight variation in ring width/thickness, accounting for the slight shifts in the field. Additionally, remanence in the iron cores of the electromagnets used to generate the applied fields in the experimental data may have led to slightly asymmetrical field rotations, which could explain biasing in the formation of vortex states in the experimental data, which is not seen in the model. However, in combination with the previously presented results, there is strong evidence that RingSim provides an excellent description of the overall processes that dictate the response of the magnetic nanoring arrays.

## VII. CONCLUSIONS

In this paper, we have outlined an agent-based methodology for modeling extended nanowire networks. With a combination of analytical models for calculating reversal probabilities and directly

programmed phenomenological behavior, RingSim was able to emulate the behaviors observed in real nanoring devices.

The resulting model provides excellent agreement with experimentally gathered data, not only in the global response of the system following equilibration of its DW population, but also with the dynamic timescales associated with reaching the equilibrium as well as the typical domain microstates that are formed across different driving fields. RingSim is able to model relatively large areas of magnetic materials with modest computational overheads, allowing predictions to be made that would be practically impossible to achieve with general-purpose micromagnetic simulators. As a rough benchmark of performance, RingSim is able to simulate the response of a  $25 \times 25$  array of nanorings at speeds of 1.4 rotations/s on an Intel i5 processor, allowing rapid evaluation of a device response to arbitrary field inputs.

The system studied here exhibits a relatively simple set of interactions that govern the depinning dynamics, namely, between externally applied fields and an energy landscape that is predominantly defined by material properties and geometry of the system. For more complex systems, such as cases where there are magneto-static interactions between multiple magnetic layers or DMI interactions at interfaces, further classes of agents, which aim to phenomenologically describe these interactions, must be included to capture their effect on system evolution.

While the exact formulation and phenomenology featured within RingSim is specific to the system of interconnected magnetic nanorings, simple phenomenological simulators are useful tools for approximating device-level behaviors. Provided that the phenomenological descriptions of underlying processes can accurately capture key behaviors, we believe that similar methodologies can be applied to other simple systems. In particular, these approaches are well-suited to studying DW dynamics in other systems of interconnected magnetic nanowires. Thus, simulation tools, such as RingSim, can be useful for rapid exploration of mesoscale device behaviors beyond the speed of conventional simulation approaches.

## ACKNOWLEDGMENTS

The authors thank STFC for beam time on beamline I06 at the Diamond Light Source and thank Jordi Prat, Michael Foerster, and Lucia Aballe from ALBA for providing quadrupole sample holders.<sup>37</sup> I.T.V. acknowledges DTA-funded Ph.D. studentships from EPSRC. The authors gratefully acknowledge the support of EPSRC through grants EP/S009647/1, EP/V006339/1, and EP/V006029/1. This project has received funding from the European Union’s Horizon 2020 FET-Open program under Grant Agreement No. 861618 (SpinEngine) and the Leverhulme Trust (No. RPG-2018-324).

## AUTHOR DECLARATIONS

### Conflict of Interest

The authors have no conflicts to disclose.

### Author Contributions

I.T.V. designed and programmed RingSim and performed all simulations with RingSim. MuMax simulations were performed by I.T.V. and G.V. G.V. performed quantitative analysis on X-PEEM images. D.G. helped optimize the speed of the model. I.T.V.,

14 May 2025 09:28:52



G.V., and C.S. designed the setup for performing AMR measurements. I.T.V. performed all AMR measurements. G.V., C.S., and P.W.F. designed and manufactured all samples. I.T.V., R.M.R.-R., A.W., T.J.H., and D.A.A. performed X-PEEM measurements, which were overseen by F.M. and S.S.D. D.A.A. and T.J.H. conceptualized the work.

**Ian T. Vidamour:** Formal analysis (lead); Investigation (lead); Methodology (lead); Software (lead); Validation (lead); Visualization (lead); Writing – original draft (lead); Writing – review & editing (equal). **Guru Venkat:** Formal analysis (supporting); Investigation (supporting); Methodology (supporting); Software (supporting); Writing – review & editing (equal). **Charles Swindells:** Investigation (supporting); Methodology (supporting); Writing – review & editing (equal). **David Griffin:** Software (supporting). **Paul W. Fry:** Resources (supporting). **Richard M. Rowan-Robinson:** Investigation (supporting). **Alexander Welbourne:** Investigation (supporting). **Francesco Maccherozzi:** Resources (supporting). **Sarnjeet S. Dhesi:** Resources (supporting). **Susan Stepney:** Funding acquisition (equal); Writing – review & editing (equal). **Dan A. Allwood:** Conceptualization (equal); Funding acquisition (supporting); Investigation (supporting); Methodology (supporting); Supervision (supporting). **Thomas J. Hayward:** Conceptualization (equal); Formal analysis (supporting); Funding acquisition (lead); Investigation (supporting); Methodology (supporting); Supervision (lead); Writing – original draft (supporting); Writing – review & editing (equal).

## DATA AVAILABILITY

The data that support the findings of this study are available from the corresponding author upon reasonable request. The simulation packages used to generate these data are available at <https://github.com/ianvidamour/RingSim>.

## REFERENCES

- <sup>1</sup>J. Torrey et al., “Neuromorphic computing with nanoscale spintronic oscillators,” *Nature* **547**, 428–431 (2017).
- <sup>2</sup>T. Kanao et al., “Reservoir computing on spin-torque oscillator array,” *Phys. Rev. Appl.* **12**, 024052 (2019).
- <sup>3</sup>A. Pivano and V. O. Dolocan, “Chaotic dynamics of magnetic domain walls in nanowires,” *Phys. Rev. B* **93**, 144410 (2016).
- <sup>4</sup>R. V. Ababei et al., “Neuromorphic computation with a single magnetic domain wall,” *Sci. Rep.* **11**, 15587 (2021).
- <sup>5</sup>A. Welbourne et al., “Voltage-controlled superparamagnetic ensembles for low-power reservoir computing,” *Appl. Phys. Lett.* **118**, 202402 (2021).
- <sup>6</sup>A. Vansteenkiste et al., “The design and verification of MuMax3,” *AIP Adv.* **4**, 107133 (2014).
- <sup>7</sup>M. J. Donahue and D. G. Porter, “OOMMF user’s guide,” version 1.0, 1999.
- <sup>8</sup>L. Landau and E. Lifshitz, “On the theory of the dispersion of magnetic permeability in ferromagnetic bodies,” in *Perspectives in Theoretical Physics* (Elsevier, 1992), pp. 51–65.
- <sup>9</sup>T. L. Gilbert, “A Lagrangian formulation of the gyromagnetic equation of the magnetization field,” *Phys. Rev.* **100**, 1243 (1955).
- <sup>10</sup>X. Chen et al., “Forecasting the outcome of spintronic experiments with neural ordinary differential equations,” *Nat. Commun.* **13**, 1016 (2022).
- <sup>11</sup>J. Leliaert and J. Mulders, “Tomorrow’s micromagnetic simulations,” *J. Appl. Phys.* **125**, 180901 (2019).
- <sup>12</sup>S. H. Skjærvø, C. H. Marrows, R. L. Stamps, and L. J. Heyderman, “Advances in artificial spin ice,” *Nat. Rev. Phys.* **2**, 13–28 (2020).
- <sup>13</sup>R. W. Dawidek et al., “Dynamically-driven emergence in a nanomagnetic system,” *Adv. Funct. Mater.* **31**, 2008389 (2021).
- <sup>14</sup>J. H. Jensen and G. Tufte, “Reservoir computing with a chaotic circuit,” in *ECAL 2017, the Fourteenth European Conference on Artificial Life* (MIT Press, 2017), pp. 222–229; see [https://doi.org/10.1162/isal\\_a\\_039](https://doi.org/10.1162/isal_a_039).
- <sup>15</sup>J. H. Jensen and G. Tufte, “Reservoir computing in artificial spin ice,” in *ALIFE 2020: The 2020 Conference on Artificial Life* (MIT Press, 2020), pp. 376–383; see [https://doi.org/10.1162/isal\\_a\\_00268](https://doi.org/10.1162/isal_a_00268).
- <sup>16</sup>J. C. Gartside et al., “Reconfigurable training and reservoir computing in an artificial spin-vortex ice via spin-wave fingerprinting,” *Nat. Nanotechnol.* **17**, 460–469 (2022).
- <sup>17</sup>K. Hon et al., “Numerical simulation of artificial spin ice for reservoir computing,” *Appl. Phys. Express* **14**, 033001 (2021).
- <sup>18</sup>K. D. Stenning et al., “Adaptive programmable networks for in materia neuro-morphic computing,” *arXiv:2211.06373* (2022).
- <sup>19</sup>I. Vidamour et al., “Quantifying the computational capability of a nanomagnetic reservoir computing platform with emergent magnetisation dynamics,” *Nanotechnology* **33**, 485203 (2022).
- <sup>20</sup>I. Vidamour et al., “Reconfigurable reservoir computing in a magnetic meta-material,” *Commun. Phys.* **6**, 230 (2023).
- <sup>21</sup>G. Venkat et al., “Exploring physical and digital architectures in magnetic nanoring array reservoir computers,” *Neuromorphic Comput. Eng.* **4**(2), 024018 (2024).
- <sup>22</sup>C. M. Macal and M. J. North, “Agent-based modeling and simulation,” in *Proceedings of the 2009 Winter Simulation Conference (WSC)* (IEEE, 2009), pp. 86–98; see <https://doi.org/10.1109/WSC.2009.5429318>.
- <sup>23</sup>F. Stonedahl and U. Wilensky, “Finding forms of flocking: Evolutionary search in ABM parameter-spaces,” in *Multi-Agent-Based Simulation XI: International Workshop, MABS 2010, Toronto, Canada, 11 May 2010, Revised Selected Papers 11* (Springer, 2011), pp. 61–75.
- <sup>24</sup>K. E. Joyce, P. J. Laurienti, and S. Hayasaka, “Complexity in a brain-inspired agent-based model,” *Neural Netw.* **33**, 275–290 (2012).
- <sup>25</sup>L. Zhang, C. G. Strouthos, Z. Wang, and T. S. Deisboeck, “Simulating brain tumor heterogeneity with a multiscale agent-based model: Linking molecular signatures, phenotypes and expansion rate,” *Math. Comput. Model.* **49**, 307–319 (2009).
- <sup>26</sup>L. J. Chang, Y. D. Yao, P. Lin, and S. F. Lee, “Magnetic interaction in domain wall depinning at square notch and antinotch traps,” *IEEE Trans. Magn.* **47**, 2519–2521 (2011).
- <sup>27</sup>C. W. Sandweg et al., “Direct observation of domain wall structures in curved permalloy wires containing an antinotch,” *J. Appl. Phys.* **103**, 93906 (2008).
- <sup>28</sup>C. Vogler, F. Bruckner, D. Suess, and C. Dellago, “Calculating thermal stability and attempt frequency of advanced recording structures without free parameters,” *J. Appl. Phys.* **117**, 163907 (2015).
- <sup>29</sup>J. W. Lau, M. Beleggia, and Y. Zhu, “Common reversal mechanisms and correlation between transient domain states and field sweep rate in patterned permalloy structures,” *J. Appl. Phys.* **102**, 043906 (2007).
- <sup>30</sup>W. Wernsdorfer et al., “Experimental evidence of the Néel-Brown model of magnetization reversal,” *Phys. Rev. Lett.* **78**, 1791–1794 (1997).
- <sup>31</sup>M. Negoita, T. J. Hayward, and D. A. Allwood, “Controlling domain walls velocities in ferromagnetic ring-shaped nanowires,” *Appl. Phys. Lett.* **100**, 072405 (2012).
- <sup>32</sup>M. Negoita, T. J. Hayward, J. A. Miller, and D. A. Allwood, “Domain walls in ring-shaped nanowires under rotating applied fields,” *J. Appl. Phys.* **114**, 013904 (2013).
- <sup>33</sup>M. P. Sharrock, “Time dependence of switching fields in magnetic recording media (Invited),” *J. Appl. Phys.* **76**, 6413–6418 (1994).
- <sup>34</sup>J.-E. Wegrowe et al., “Magnetic relaxation of nanowires: Beyond the Néel-Brown activation process,” *Europhys. Lett.* **38**, 329 (1997).
- <sup>35</sup>S. Dutta, S. A. Siddiqui, J. A. Currivan-Incorvia, C. A. Ross, and M. A. Baldo, “The spatial resolution limit for an individual domain wall in magnetic nanowires,” *Nano Lett.* **17**, 5869–5874 (2017).
- <sup>36</sup>G. Venkat et al., “Peem-data-analysis,” (2021); see <https://gitlab.com/spintronic-computing-group/data-analysis/peem-data-analysis>.
- <sup>37</sup>M. Foerster et al., “Custom sample environments at the ALBA XPEEM,” *Ultramicroscopy* **171**, 63–69 (2016).

14 May 2025 09:28:52